Automated Whole Slide Imaging for Label-Free Histology Using Photon Absorption Remote Sensing Microscopy

James E.D. Tweel, Benjamin R. Ecclestone, Marian Boktor, Deepak Dinakaran, John R. Mackey, and Parsin Haji Reza

Abstract*—*Objective: **Pathologists rely on histochemical stains to impart contrast in thin translucent tissue samples, revealing tissue features necessary for identifying pathological conditions. However, the chemical labeling process is destructive and often irreversible or challenging to undo, imposing practical limits on the number of stains that can be applied to the same tissue section. Here we present an automated label-free whole slide scanner using a PARS microscope designed for imaging thin, transmissible samples. *Methods*: Peak SNR and in-focus acquisitions are achieved across entire tissue sections using the scattering signal from the PARS detection beam to measure the optimal focal plane. Whole slide images (WSI) are seamlessly stitched together using a custom contrast leveling algorithm. Identical tissue sections are subsequently H&E stained and brightfield imaged. The one-to-one WSIs from both modalities are visually and quantitatively compared. *Results*: PARS WSIs are presented at standard 40x magnification in malignant human breast and skin samples. We show correspondence of subcellular diagnostic details in both PARS and H&E WSIs and demonstrate virtual H&E staining of an entire PARS WSI. The one-to-one WSI from both modalities show quantitative similarity in nuclear features and structural information. *Conclusion*: PARS WSIs are compatible with existing digital pathology tools, and samples remain suitable for histochemical, immunohistochemical, and other staining techniques. *Significance*: This work is a critical advance for integrating label-free optical methods into standard histopathology workflows.**

***Index Terms*—Digital pathology, label-free optical methods, photon absorption remote sensing, virtual histology, whole slide imaging.**

I. Introduction

HISTOLOGY is the study of microscopic cell structure and function and is critical in understanding the biological processes that underlie health and disease [1]. Histopathologists use a variety of staining techniques on tissue samples to highlight tissue structure and composition, and to localize different biomolecules such as proteins, lipids, and carbohydrates. For example, nuclear stains, such as DAPI and hematoxylin, provide visualizations of nuclear morphology (e.g., size, shape) and insights into cellular organisation, growth, proliferation, and more [2], [3], [4]. These features are used to distinguish healthy and abnormal biological function, helping pathologists grade the presence, nature, and extent of a disease. Therefore, nuclear stains serve as a fundamental contrast for various histological analyses. The gold standard stain in histology combines hematoxylin and eosin (H&E), wherein hematoxylin stains the chromatin in the nuclei purple and eosin stains the cytoplasm and extracellular matrix (ECM) structures pink [5]. There are also specialized stains, such as Masson's trichrome and periodic acid Schiff, capable of targeting more specific tissue structures [6]. In addition, more advanced techniques such as immunohistochemical staining and *in-situ* hybridization are available for localization of specific proteins and DNA/RNA sequences, respectively [6].

Stains are applied to thinly sliced ($\sim$5 μm) translucent tissue sections which are then imaged for microscopic inspection using brightfield or fluorescent whole-slide scanners [1], [5]. These microscopes capture the entire tissue area, generating a large gigapixel-sized whole slide image (WSI) which is viewable at both low and high magnifications. The multi-viewing capability of WSIs is crucial for a thorough diagnosis, enabling pathologists to overview the sample and identify regions of interest (ROIs) that require detailed examination [7], [8]. Moreover, observing the entire specimen helps pathologists identify

Manuscript received 16 August 2023; revised 18 December 2023; accepted 12 January 2024. Date of publication 17 January 2024; date of current version 13 May 2024. This work was supported in part by the Natural Sciences and Engineering Research Council of Canada under Grants DGECR-2019-00143, RGPIN2019-06134, and DH-2023-00371, in part by the Canada Foundation for Innovation under JELF Grant 38000, in part by Mitacs Accelerate under Grant IT13594, in part by the University of Waterloo Startup Funds, Centre for Bioengineering and Biotechnology (CBB Seed fund), illumiSonics Inc under SRA Grant 083181, in part by New Frontiers in Research Fund – Exploration under Grant NFRFE-2019-01012, and in part by the Canadian Institutes of Health Research under Grant CIHR PJT 185984. *(Corresponding author: Parsin Haji Reza.)*

James E.D. Tweel and Benjamin R. Ecclestone are with the Photomedicine Labs, Systems Design Engineering Department, University of Waterloo, Canada, and also with the Illumisonics Inc., Canada.

Marian Boktor is with the Photomedicine Labs (PML), Systems Design Engineering Department, University of Waterloo, Canada.

Deepak Dinakaran is with the Department of Radiation Oncology, Sunnybrook Health Sciences Centre, University of Toronto, Canada, and also with the Illumisonics Inc., Canada.

John R. Mackey is with the Illumisonics Inc., Canada.

Parsin Haji Reza is with the Photomedicine Labs, Systems Design Engineering Department, University of Waterloo, Waterloo, ON N2L 3G1, Canada (e-mail: phajirez@uwaterloo.ca).

Digital Object Identifier 10.1109/TBME.2024.3355296

dispersed disease patterns and abnormalities, which may easily be missed when examining only a zoomed-in section. As a result, whole slide imaging techniques are crucial for thorough clinical assessment.

While staining methods and advanced labeling techniques continue to prove invaluable in providing insights for medicine and disease, they are not without their limitations. Histological processing steps can be time-consuming, resource intensive, and require trained histotechnologists [9]. For example, prior to staining, fresh tissue samples undergo formalin fixation, dehydrated, and paraffin embedding before being thinly sliced onto microscope slides [1], [5]. In oncology, this can present a significant obstacle to achieving a prompt diagnosis [10]. Additionally, the chemical labeling process is destructive and can be irreversible or challenging to undo [11]. Consequently, the process of 'destaining' is not always practical or achievable, thereby limiting the number of stains that may be simultaneously or sequentially applied on the same tissue section (i.e., stain multiplexing) [11], [12]. In practice, a new section is often required for each staining protocol. However, cutting multiple sections may not be feasible, especially in valuable biopsy samples (e.g., brain tissue, needle biopsies) which should be used sparingly.

Label-free imaging techniques present a promising approach to alleviate or circumvent some of the aforementioned challenges, while also complementing traditional histology methods. Such techniques are capable of acquiring contrast in a sample based on its inherent optical properties without the use of chemical labels (e.g., stains or fluorescent dyes) [13]. Depending on the method employed, the obtained contrasts may offer analogous information (e.g., nuclear visualizations) to certain stains, such as H&E or DAPI. Additionally, these label-free contrasts may be intelligently combined or virtually stained using deep-learning models, enabling the emulation of histological [14], [15], [17] or immunobiological-like [18] stains. This virtual staining approach has the potential to reduce preparation time and resource costs associated with certain stains. Moreover, the unstained tissue section may be used in conjunction with existing staining protocols if specific molecular analyses are needed.

Broadly speaking, current label-free methods use scattering and absorption processes to provide contrast in biological specimens. Scattering techniques such as optical coherence tomography (OCT) [19], [20], [21], [22] and quantitative phase imaging (QPI) methods [16], [23], [24], [25] have been investigated for label-free tissue histology. However, their diagnostic utility largely depends on interpreting morphological features alone, as tissue scattering properties lack biomolecular specificity [19], [24].

In contrast, absorption-based microscopy techniques target biomolecules based on their absorption spectra and generate contrast through radiative or non-radiative relaxation processes [26], [27]. Radiative absorption contrast has been realized in autofluorescence microscopy [14], [15], [28], [29], along with various non-linear label-free microscopy techniques, employed independently [30], [31], [32], [33], [34] and in multimodal configurations [35], [36], for stain-free histology purposes. Radiative emissions from endogenous fluorophores, often excited with ultraviolet (UV) or shorter visible wavelengths [37], provides visualizations of ECM structures and functional characteristics of biological specimen [28], [37], [38]. However, chromatin (DNA, RNA) has relatively low quantum yield [39] and therefore important nuclear contrast is absent in autofluorescence techniques.

Non-radiative absorption contrast has been achieved with photothermal [40], [41] and photoacoustic (PA) [42], [43], [44] imaging techniques for label-free histology-like visualizations. Photoacoustic remote sensing was first used for label-free nuclear imaging in unstained tissues by Haven et al. [45] and Abassi et al. [46] in 2019. It has also been used to image a variety of biomolecules label-free including hemoglobin [47], [48], [49], [50], [51], cytochromes [52], [53], DNA/RNA and lipids [54], [55]. More recently, Ecclestone et al. [56] presented the next generation method, now called photon absorption remote sensing (PARS), capable of simultaneously capturing scattering, radiative (autofluorescence) and non-radiative relaxation contrasts.

PARS captures these relaxation contrasts following a single absorption event from a pulsed excitation laser. Following absorption, all optical emissions from the radiative relaxation process are broadly captured while heat and pressure, from the non-radiative process, modulate the sample's local optical properties. Non-radiative contrast is derived from the resulting intensity modulations (photothermal and photoacoustic signals) of a secondary co-focused detection beam's backscattered light [56]. Prior to excitation, this backscattered light is used to capture scattering contrast of the sample.

Here we present an automated whole slide scanning PARS microscope with an optical architecture designed to take advantage of forward scattering in thin, transmissible samples. The capacity to obtain automated whole slide images of tissues sections has not yet been achieved using the PARS imaging technology. We employ a free-space, non-confocal detection pathway to capture forward scattered light and radiative emissions from the entire depth of the thin tissue samples. Additionally, we have added a spectral filter to separate the forward detection beam and radiative emission spectrum. Beam samplers have been incorporated into the PARS optical system to measure incident detection power and excitation pulse energies. These measurements allow us to reduce image noise by correcting for power instabilities during imaging.

These optics refinements facilitate histology-like label-free whole slide imaging, and importantly, allow for a significant reduction in detection powers and ultraviolet excitation energy compared to recent PARS histology implementations [57], [58]. With these reduced powers, the unstained tissue sections remain unaltered and available for subsequent standard histochemical staining, enabling us to showcase both PARS and H&E whole slide images of the same tissue section in malignant human breast and skin samples. This ability to acquire one-to-one WSIs of both modalities is crucial for benchmarking diagnostic performance and concordance with gold standards.

The PARS whole slide scanning workflow introduced in this study uses all three PARS contrasts, with the scattering channel playing a crucial role in enabling the acquisition of in-focus, high quality images across an entire tissue sample. Samples are automatically scanned in parts and precision-focus is achieved

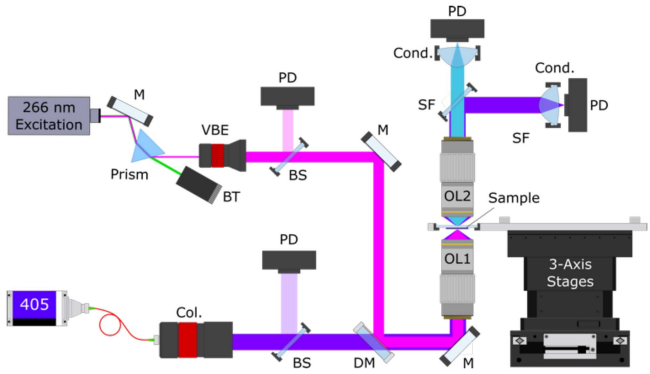

Fig. 1. Simplified PARS histology optical architecture. Component labels are defined as follows: mirror, *M*; dichroic mirror, *DM*; variable beam expander, *VBE*; collimator, *Col.*; condenser lens, *Cond.*; spectral filter, *SF*; beam sampler, *BS*; photodiode, PD; objective lens, OL.

for each section using an autofocusing algorithm. This strategy ensures the maintenance of accurate focus across the entire sample. The individually scanned sections are then seamlessly stitched together using a novel contrast leveling algorithm, forming a comprehensive whole slide image. Additionally, we also show, for the first time, virtual H&E staining of a whole slide PARS image. To reinforce the visual similarities between the PARS and H&E WSIs, we performed a feature-based quantitative comparison between the modalities, wherein nuclear featuring such as nuclear count, area, and eccentricity are compared. Furthermore, a multi-scale structural similarity index measure (MS-SSIM) is used to compare the virtual and real H&E WSI pairs at increasing pathology magnifications.

The whole slide images presented here allow for examination of tissue structures at resolutions sufficient for the recovery of diagnostically relevant subcellular details. Crucially, they provide pathologists with the necessary magnification range (up to 40x) to allow for comprehensive analysis of entire tissue samples, at both low and high magnifications, for informed and accurate diagnosis. The label-free slide images exhibit contrasts analogous to gold standard H&E stained slides and are viewable using the same or similar existing digital pathology tools.

II. Methods

A. PARS Histology System Architecture

The PARS histology imaging system architecture is shown in Fig. 1. For the excitation laser, a 50 KHz 400 ps pulsed 266 nm UV laser (Wedge XF 266, RPMC) was chosen. This excitation wavelength is used to target the optical absorption of DNA, facilitating label-free nuclear contrast through non-radiative relaxation [59]. Additionally, it offers contrast for various structures of the extracellular matrix through the radiative relaxation process [28], [37], [38].

At the output of the 266 nm source, a CaF_2 prism (Prism: PS862, Thorlabs) is used to remove residual 532 nm light and send it to a beam trap (BT: BT610, Thorlabs). The UV beam is then expanded (VBE: BE03-266, Thorlabs) and combined with the detection pathway using a long-pass dichroic mirror (DM: 37–721, Edmund optics).

For the detection path, a continuous wave 405 nm laser (OBIS-LS 405, Coherent), first reported in [56], was chosen. The 405 nm wavelength tightly overlaps with the excitation source focus spot, enabling effective probing of the excited area [56]. Furthermore, the 405 nm wavelength has good chromatic compatibility with the UV excitation source. The output of the fiber-coupled detection source is collimated (Col: C40APC-A, Thorlabs) and then directed through the dichroic mirror to join the UV beam.

The co-aligned detection and excitation beams are then focused onto the sample with a 0.42 numerical aperture (NA) UV objective lens (OL1: NPAL-50-UV-YSTF, OptoSigma). The transmitted detection light and forward emissions from the radiative relaxation process are collected using a 0.7 NA objective lens (OL2: 278-806-3, Mitutoyo) and then separated with a 405 nm notch filter (SF: NF405-13, Thorlabs). The detection intensity modulations and radiative emissions are then each recorded on an avalanche photodiode (PD: APD130A2) following condenser lenses (Cond: ACL25416 U-A, Thorlabs). Prior to excitation and detection co-alignment, beam samplers (BSF10-UV/A, Thorlabs) are used to sample a portion of both the detection power and excitation pulse energy for reference and post-acquisition correction purposes.

B. Whole Slide Scanning Workflow

The PARS histology system first captures a preview image of the whole slide to allow the user to trace a border around the entire sample or draw a smaller region of interest (ROI). These ROI coordinates are mapped to mechanical stage positions to inform the scanning algorithm of the tissue boundaries. To calibrate the mapping between the preview image's pixel coordinates and the stage coordinates, images of a USAF resolution target are captured from both the preview camera and the PARS system. Alignment points between the images are used to determine a linear transform between the two coordinate spaces.

The optimal focus plane must be maintained across the entire sample in order to acquire consistent high quality raw data. To do so, the selected area is split into smaller (typically $\sim$0.5 mm^2) square sections (S_n) as shown in Fig. 2(a). Before scanning each section, the axial (z) stage is adjusted to pinpoint the sharpest imaging plane. This involves scanning a small portion of the section across depth and assessing sharpness using the Tenengrad focus measure. Once the optimal position is identified, the entire section is scanned at this axial depth. With this approach, the system is able to compensate for variances in the sample's surface morphology and is robust to any tilt in the sample and scanning plane. Some sections positioned at the edge of the sample may cover more glass area than tissue area. This may cause the optimal focus to skew towards particles on the glass surface rather than tissue layer. As such, these sections are flagged (blue in Fig. 2(a)) and will be scanned at the optimal focus of the closest adjacent section with sufficient tissue coverage (red in Fig. 2(a)).

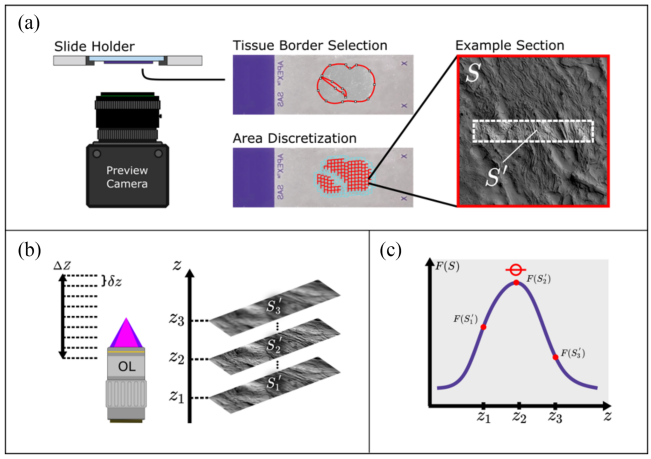

Fig. 2. Overview of the PARS whole slide scanning workflow. (a) A preview camera is used to capture an image of the slide so the tissue border can be selected, and its area split into small sections, each to be independently scanned. (b) Before imaging S_n, scattering images of subset S'_n are taken across a depth ΔZ at a step size δz. (c) A relative focus metric is plotted for each scattering image from (b), and an optimal focus metric is determined.

C. Focus Criterion Function and Autofocus Algorithm

To find the optimal plane of focus for each section, a small sampling of the section area (S'_n) is imaged multiple times across a depth of ΔZ at step sizes of δz, as shown in Fig. 2(b). With a smaller step size (δz), the selected maximum focus will better approximate the exact peak location. With a greater search depth (ΔZ), a larger focal shift can be accommodated between neighbouring sections. In this study, the search depth (ΔZ) was set at 4.5 μm, which is both close to the thickness of the tissue sections ($\sim$5 μm) and the Abbe theoretical axial resolution ($\sim$4.591 μm) for the 405 nm detection beam and 0.42 NA objective lens. The step size (δz) was set to 0.5 μm to provide sufficient step resolution to approximate the peak. While finer step sizes could be set, it would significantly increase autofocusing time with minimal benefit. Overall, with these selected values, each autofocus search required a total of N = 10 focus points (0 μm to 4.5 μm inclusive).

For the subsections imaged across depth, the detection beam alone is sufficient for finding peak focus for all image channels (scattering, radiative and non-radiative). The Tenengrad focus criterion function is then used to evaluate the relative sharpness of the scattering images acquired across depth. The Tenengrad function was chosen because it provides a sharp peak for fine focusing and is relatively noise robust [60]. It first computes the horizontal (G_x) and vertical gradients (G_y) of an input image (I) at point (x, y) using the Sobel kernels:

$$G_x = \begin{bmatrix} 1 & 0 & -1 \\ 2 & 0 & -2 \\ 1 & 0 & -1 \end{bmatrix} * I \quad \text{and} \quad G_y = \begin{bmatrix} 1 & 2 & 1 \\ 0 & 0 & 0 \\ -1 & -2 & -1 \end{bmatrix} * I \tag{1}$$

From here the gradient magnitude, $G(x, y)$, is computed:

$$G\ (x, y) = \sqrt{G_x^2\ (x, y) + G_y^2\ (x, y)} \tag{2}$$

The focus criterion function, $f(I)$, is then evaluated as the sum of squared gradient magnitude values which exceed a given threshold T:

$$F\ (I) = \sum_x \sum_y \left[G\ (x, y)\right]^2 \forall\ G\ (x, y) > T \tag{3}$$

The Tenengrad function quantifies the magnitude of the edges present in the scene. Across depth, it will produce a plot similar to Fig. 2(c), with a single peak which monotonically decreases as the sample moves above or below this point. At the beginning of the whole slide scan, a course focus search is deployed over a large range to determine a rough starting point for the slide. Following this, subsequent section foci are found by quadratically interpolating the evaluated depth stack (N = 10) centered at the optimal focus point of the closest neighbouring section. The computation time for the Tenengrad function depends on the size of the evaluated image. Here the subsections (S'_n) are 0.5 mm $\times$ 15 μm or 3% of the full 0.5 mm $\times$ 0.5 mm section area. For this size, the Tenengrad function takes $\sim$5ms per depth scan or 0.05 s across all 10 depth scans.

D. Section Scanning and Image Reconstruction

During imaging, mechanical stages continually move the sample over the objective lens in an 's' or 'snake'-like scan pattern. Sample points are spaced out laterally to achieve the desired 40x equivalent magnification ($\sim$250 nm/pixel). At each excitation event, a high-speed digitizer (CSE1442, RZE-004-200, Gage Applied) captures the stage position information as well as $\sim$500 ns of time resolved data from each system photodiode. These signals are then compressed into single amplitude values for the non-radiative, radiative, and scattering image channels. In addition, the 266 nm excitation pulse energy and 405 nm detection power are also simultaneously collected at this location. To form the non-radiative, radiative, and scattering images, the raw data points are arranged as pixels on a cartesian grid based on their stage position. The radiative and non-radiative images are then power corrected using the 266 nm pulse energy measurement. Similarly, the scattering image is power corrected using the 405 nm detection power measurement.

E. Whole Slide Stitching and Contrast Leveling Algorithm

After all sections are scanned, they can be stitched together into a whole slide image using their relative stage positions. However, prior to stitching, a contrast and brightness leveling algorithm is needed to blend the shading differences between adjacent sections. The algorithm is two part, consisting of a bulk leveling stage (Fig. 3(a)) and gradient leveling stage (Fig. 3(b)). Both parts use a small amount of overlap ($\sim$100 pixels per direction) between sections to help with the blending. The bulk leveling algorithm brings all sections into the same overall brightness and contrast range while the gradient leveling algorithm blends the sharp transitions between sections due mismatched gradients of illuminations.

In bulk leveling, the inner and outer overlap areas are used to determine a transform ($T_{\mu\sigma_{i/o}}$) to level the inner section. This

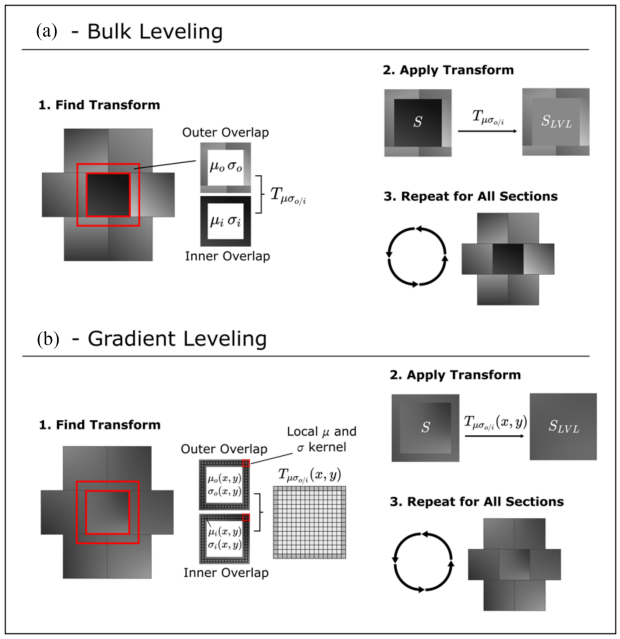

Fig. 3. Illustration of the two-part algorithm used to level and blend the contrast and shading between sections. (a) Bulk leveling algorithm aims to bring all sections into the same general contrast range. Here a single transform ($T_{\mu\sigma_{o/i}}$) for the entire inner section is derived based on the overlap area between the inner and outer sections. (b) A gradient leveling algorithm aimed at continuously blending the boundaries between neighboring sections. Here a point transform ($T_{\mu\sigma_{o/i}}(x,y)$) for the inner section is derived based on a comparison between the local statistics of the grayscale values of inner and outer overlap regions.

transform is based on the mean and standard deviation of the inner (μ_i, σ_i) and outer overlap pixels (μ_o, σ_o).

$$S_{LVL} = T_{\mu\sigma_{i/o}}(S) = \frac{\sigma_o}{\sigma_i} * (S - \mu_i) + \mu_o \tag{4}$$

Equation (4) scales the inner section's pixel intensity spread to better match the outer section based on the ratio of the outer and inner overlap standard deviations. It then shifts the average pixel intensity of the inner section (S) to the average pixel intensity of the outer section overlap. This is then repeated for every section in the whole slide image before moving on to the gradient leveling algorithm. For gradient leveling, a kernel with a size equal to the overlap, computes a local mean and standard deviation value at each point along the inner and outer overlaps. Values in non-overlap locations are interpolated using values from surrounding overlap areas. These local statistic values are used to create a point transform, $T_{\mu\sigma_{i/o}}(x,y)$, which has the same form as (4) but varies at each pixel location. The transform values are then Gaussian blurred and applied to the inner section. This is then repeated for every section in the whole slide image. In some cases, the bulk or gradient leveling algorithm may be repeated more than once until the mosaic artifacts are corrected.

F. Quantitative Analysis of Image Similarity

To quantitatively compare the similarity between the PARS and H&E images, nuclear features, including nuclei count, nuclear area, and nuclear eccentricity were computed. The nuclear features were extracted from N = 1793 PARS and H&E sample pairs (each of size 512x512 pixels) sourced from the skin and breast whole slide tissue samples used in this study. Nuclear segmentation was performed in each image type using the StartDist python library [61]. For the PARS images, nuclear segmentation was done on the non-radiative channel, which primarily highlights nuclear structures. For the brightfield H&E images, a color deconvolution algorithm [62] was first used to isolate the hematoxylin channel and facilitate nuclear segmentation. The hematoxylin channel was then inverted, and contrast enhanced by rescaling pixel intensities. The minimum and maximum threshold bounds for this rescaling were determined manually for each whole slide image. The nuclei count, average nuclear area, and average nuclear eccentricity were then extracted from the 512x512 pixel segmentation maps using the *regionprops* function from the skimage Python library.

This same feature-based evaluation was applied to compare the virtual and real H&E whole slide image pair (N = 383). Additionally, the multi-scale structural similarity index measure (MS-SSIM) was employed as a pixel-level quantitative measure of agreement. Following the methodology in [58], RGB images were converted to the YC_bC_r color space, and the MS-SSIM metric was computed for each channel and summed together with the following weights: 0.8 (Y), 0.1 (C_b), and 0.1 (C_r). This process was performed for the native PARS 40x magnification and was repeated for 20x, 10x, and 5x equivalent viewing magnifications. These lower magnifications were achieved by low pass filtering the original image pairs. For the pixel wise alignment, the WSIs were registered using an affine transformation.

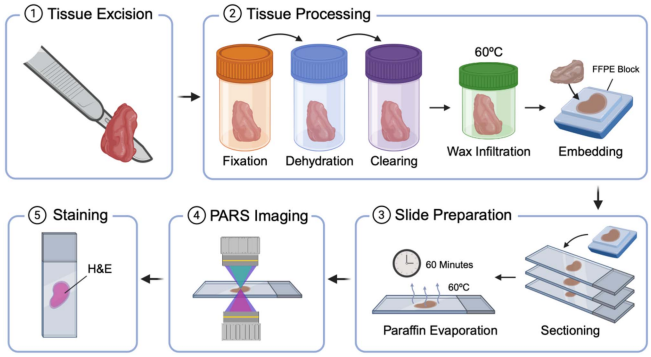

Fig. 4. Overview of the sample preparation workflow: Fresh tissue samples are first excised, processed into FFPE blocks, prepared onto microscope slides, imaged using PARS, and subsequently stained with H&E. Created with BioRender.com.

G. Sample Preparation

In this study, a variety of unstained paraffin embedded human skin and breast tissue sections were imaged on glass microscope slides. Fig. 4 outlines the steps involved in preparing the samples for PARS imaging. Fresh tissue samples are first excised and placed in a formalin fixative solution within 20 minutes of excision. The samples are fixed for a period of 24 to 48 hours and subsequently dehydrated following exposure

to ethanol. After removing water from the specimen, xylene is used to clear the tissue, eliminating any remaining ethanol and residual fats in preparation for wax infiltration. The specimen is then placed in liquid paraffin at 60 °C where it is thoroughly infiltrated with wax. The tissue samples are then embedded in a paraffin block, creating standard formalin fixed paraffin embedded tissue (FFPE) blocks. Using a microtome, thin tissue sections (∼4-5 μm) are sliced from the FFPE block surface and placed onto glass microscope slides. The tissue slides are then baked at 60 °C for ∼60 minutes to remove excess paraffin prior to imaging with the PARS system. Following PARS imaging the exact same tissue sections were stained with H&E and imaged at 40x magnification using a standard brightfield microscope (MorphoLens 1). This provided a direct one to one comparison between the PARS image data and the gold standard H&E stain.

Tissues were provided by clinical collaborators at the Cross-Cancer Institute (Edmonton, Alberta, Canada) from anonymous patient donors with all patient identification removed from the samples. Samples were archival tissues no longer required for patient diagnostic and thus patient consent was waived by the ethics committee. No information was provided to the researchers about the patient identity. Samples were collected under protocols approved by the Research Ethics Board of Alberta (Protocol ID: HREBA.CC-18-0277) and the University of Waterloo Health Research Ethics Committee (Photoacoustic Remote Sensing (PARS) Microscopy of Surgical Resection, Needle Biopsy, and Pathology Specimens; Protocol ID: 40275). All human tissue experiments were conducted in accordance with the government of Canada guidelines and regulations, such as "Ethical Conduct for Research Involving Humans (TCPS 2)".

III. Results and Discussion

A. System Improvements and Power Correction

The PARS optical architecture presented here has been designed for whole slide imaging of thin, transmissible samples. As such, we have added a high 0.7 NA secondary objective lens overtop the sample to capture and take advantage of the stronger forward 405 nm detection scattering. As well, the free-space, non-confocal detection scheme, following the secondary objective lens, allows us to capture the forward scattered light and radiative signal from the entire depth of the sample. The stronger forward scattering allows for lower detection power while maintaining similar recovery of the modulated detection signal from the non-radiative relaxation process. Specifically, in this configuration, the detection power incident on the sample during an acquisition was in the range of ∼2–5 μW compared to the previously reported value of 156 μW [56]. In addition, the pulse energies from UV source were in the range of 150–200 pJ compared to the 5 nJ excitation energies used in the most recent UV-PARS histology system [57], [58]. These pulse energies and detection powers permit standard H&E staining and clinical diagnosis following PARS imaging without any visual damage to the sample.

Separation of the 266 nm UV excitation pulse is not required in the forward path as it is absorbed by the borosilicate glass slide. For the radiative relaxation pathway, a 405 nm notch filter has been added to spectrally separate the forward detection path from the radiative emission spectrum. Another important addition to the system were the beam samplers used to record the excitation pulse energy and detection power as the samples were point scanned. Fig. 5 highlights improvements in image quality for the non-radiative, radiative, and scattering channels after power compensating the images. In the non-radiative and radiative image channels, each pixel is derived from a single excitation event. As such, pulse energy variability results in varying absorption which manifests as a speckle-type noise on a pixel or sub-resolution level. In the case of the scattering image, which are collected with a continuous wave laser, power instabilities result in slow varying intensity streaks as the sample is scanned. The non-radiative and radiative resolutions here are measured at ∼400 nm (FWHM), which roughly corresponds to standard 40x magnification in standard histopathology [63]. By using the collected excitation pulse energy and detection power measurements these artifacts can largely be removed and the 40x magnification is well maintained. Furthermore, power compensation in the detection scattering image allowed for more robust focus finding algorithm, which was important for the automated whole slide scanning reported here.

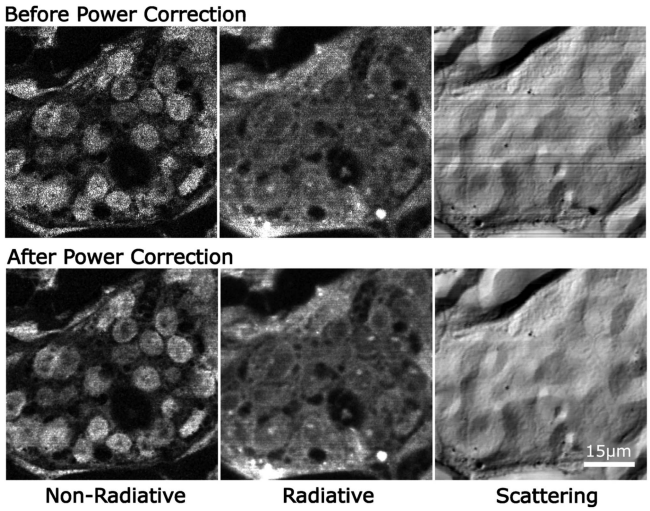

Fig. 5. Non-radiative, radiative, and scattering label-free PARS image contrasts before and after correction from the measured reference power, demonstrated on a cluster of cell nuclei.

B. Sample Autofocusing and Whole Slide Stitching

In the ideal case, the highest signal to noise ratio (SNR) and in-focus non-radiative and radiative acquisitions occurs at the optimal focus point of the detection beam. This way, the detection beam alone can be relied on for focus finding and the sample need not be exposed multiple times to UV excitation. To accomplish this, the optimal scattering focus is first determined using the methods described in Section II.C. At this peak focus, the excitation spot is moved to the optimal axial position where the largest refractive index modulation is observed. Following this axial alignment strategy, a tight correspondence between the detection focus and peak SNR of the non-radiative channel can be seen in Fig. 6(a). Here a series of scattering images are acquired across a +/− 35μm

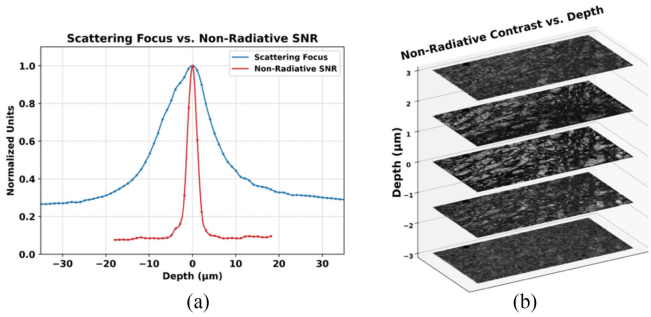

Fig. 6. Relationship between scattering focus and the non-radiative image SNR. (a) Plot of the scattering focus across depth (blue) compared with non-radiative images SNR across depth (red). (b) Visualizations of non-radiative contrast quality across a +/− 3 μm depth.

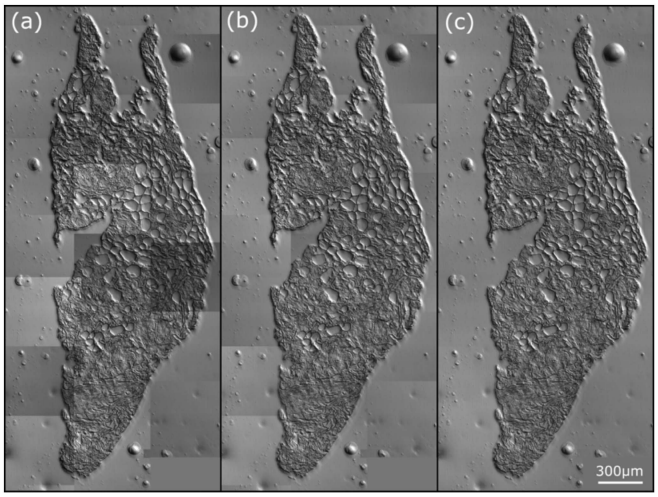

Fig. 7. Whole slide scattering image at each stage of the brightness leveling algorithm. (a) Shows the raw stitched scattering image before leveling sections. (b) Shows the stitched scattering image after bulk leveling. (c) Shows the stitched scattering image after both bulk leveling and gradient leveling.

depth range at 1μm steps. The SNR is also evaluated for a series of non-radiative images captured over a +/18 μm range at 1μm steps. Fig. 6(b) shows a stack of non-radiative images captured at and on either side (+/−1.5μm and 3μm) of the peak detection focus. Clear visual degradation of the non-radiative channel can be seen with scans taken on either side of the focus spot, which corresponds well with the sharp SNR drop on either side of the focus. Overall, Fig. 6 emphasizes and confirms the importance of maintaining focus across the entire sample. For this reason, the whole slide images are captured in discrete in-focus sections which are stitched back together.

However, the final stitched whole slide image often contains tiling artifacts between the edges of the sections. This is due to non-level illumination across sections caused by variances in tissue surface morphology. These artifacts can be corrected using the contrast leveling algorithm discussed in Section II.E, allowing for better image interpretation. Fig. 7 shows whole slide scattering images of a small breast tissue section (~3.5 × 1.2 mm^2) before and after the bulk and gradient leveling algorithms. Fig. 7(a) provides an example of the raw (pre-leveled) stitched whole slide image. In this raw image, clear brightness variations can be seen between sections and the uneven shading at section boundaries results in sharp stitching artifacts. After bulk leveling the whole slide, the obvious brightness variations between sections have largely been removed and all sections have been normalized to the same brightness range (Fig. 7(b)). However, stitching artifacts are still visible due to mismatched shading gradients between sections. After applying the gradient leveling algorithm, these sharp section transitions have been corrected giving the impression of a homogenous whole slide image (Fig. 7(c)). Overall, leveling the whole slide image is important for improving image appearance, diagnostic value, and is a critical preprocessing step for virtual staining.

C. Label-Free Whole Slide Images

When screening a biopsy sample, pathologists leverage the multi-viewing capability of whole slide images to identify diagnostically relevant regions of interest (ROIs) [7], [8]. Pathologists typically adopt a combination of two viewing strategies: 'drilling,' involving zooming in and out of an area of interest, and 'scanning,' where pathologists use a fixed zoom while panning and searching over a larger area [7]. Low magnifications allow pathologists to survey the tissue structure and cell distribution, providing the necessary context for the detailed examination of specific tissue structures at high magnification. It is therefore important to provide pathologists with entire whole slide images.

Fig. 8 shows an example whole slide image of a breast core needle biopsy with invasive ductal carcinoma. A heat map of the sample's relative focus positions is shown in Fig. 8(a), indicating the topology of the sample's surface. Each section is outlined in white and has an optimal focus assigned to its center. All other focus values are interpolated between sections. In some instances, there may be artifacts in the sample preparation process, such as dust or other particles settling on the specimen, cracks in the tissue or a small clumps of paraffin. These artifacts, while infrequent, may disrupt the autofocusing algorithm, resulting in poor image quality. However, when a focus scan fails, the algorithm will referencing the optimal focus plane of the nearest unaffected section.

Fig. 8(b) shows zoomed-out whole slide images of the non-radiative and radiative channels while Fig. 8(c) shows several higher magnification sections taken across the length of the tissue. The non-radiative channel predominantly highlights nuclear contrast while the radiative channel shows complimentary contrast of structures in the extracellular matrix. The non-radiative channel shows a high degree of variance in nuclear size, shape, and appearance, which are indicative of neoplastic features often used in the evaluation of a cancer specimen [2]. The non-radiative channel also highlights irregular loosely arranged glandular structures with a high degree of disorganisation, which are important features in grading malignancies (Fig. 8(c) blue box) [3]. The abnormal cells are seen invading and infiltrating into the surrounding stroma and adipose tissue (Fig. 8(c) red box). These visualizations, provided by the non-radiative

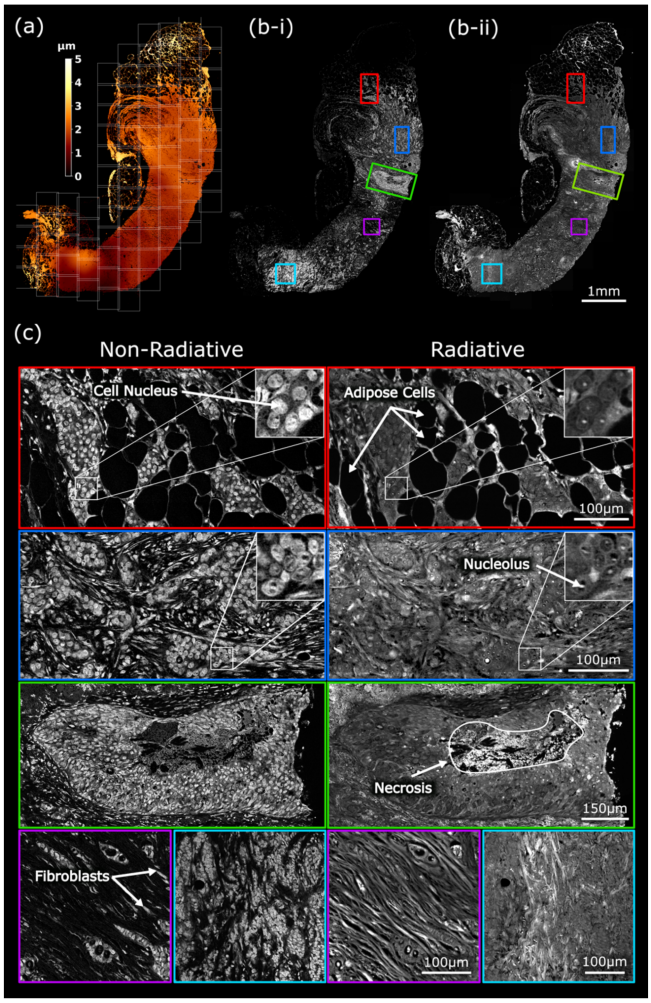

Fig. 8. Stitched and leveled PARS non-radiative and radiative whole slide images of malignant human breast tissue. (a) Shows a heat map of the relative focus positions across the sample. (b-i) and (b-ii) Show whole slide images of both non-radiative and radiative channels, respectively. (c) Shows the non-radiative and radiative contrasts at high magnification. Sections are taken from across the sample and show clinically relevant features.

channel, help pathologists determine the aggressiveness of the cancer that guides management recommendations. Furthermore, at high magnifications, subnuclear details such as nucleoli and chromatin/chromatid arrangement are seen in the radiative channel (Fig. 8(c) blue box). Such structures help show the degree of nuclear aberration and cell division (mitotic figures) in the tissue, which are important for cancer diagnosis [4]. Necrosis of breast tissue can also be seen in the radiative channel, inside a region of neoplastic cells, indicating high grade disease (Fig. 8(c), green box) [64]. Fibroblasts, which contribute to the creation of connective tissue, are also seen in the non-radiative channel. In the corresponding radiative image, these fibroblasts are embedded in long diagonal strands of connective tissue (Fig. 8(c) purple box). It's clear these label-free contrasts provide visualizations of clinically relevant features at both low and high magnifications.

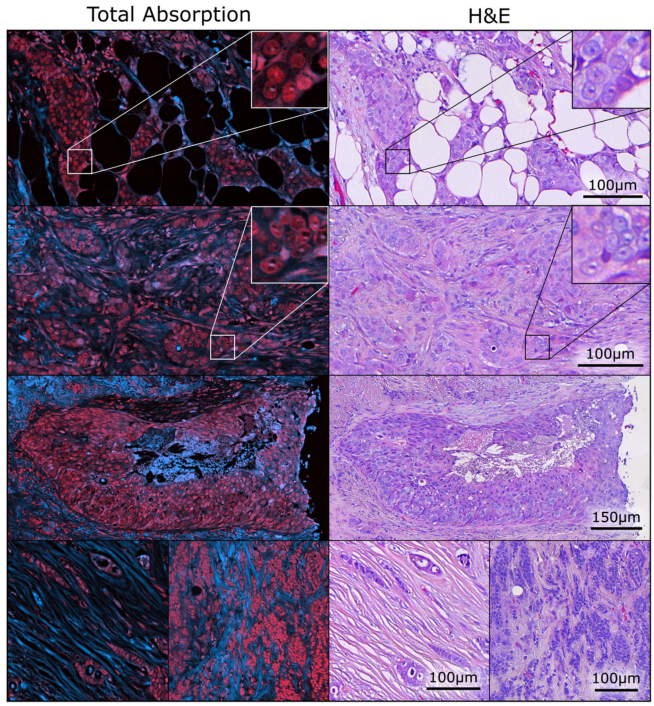

Fig. 9. One to one comparison of PARS total absorption (TA) images with the gold standard H&E stain of a breast needle core biopsy. In the colored TA image, the radiative contrast is blue and the non-radiative is red.

To further demonstrate their utility, these contrasts were combined into a single total absorption (TA) coloured image and compared against gold standard H&E staining. This one-to-one correspondence is shown in Fig. 9 for the same high magnification sections shown previously. The TA image here has the radiative channel in blue and non-radiative in red. In general, the non-radiative channel provides analogous contrast to the hematoxylin stain while the radiative channel provides analogous contrast to the eosin stain. Correspondence of the nuclear structure, shape, and size and subnuclear details is clearly seen between the TA and H&E images. Much like the combined hematoxylin and eosin stains, the combined radiative and non-radiative contrasts allow clear differentiation of various tissue types and cell structures. The potential for label-free H&E emulation is clear. The H&E images were reviewed with clinicians and found to be of diagnostic quality with no artifacts apparent from the prior PARS scanning.

Next, whole slide TA visualizations were produced to demonstrate their potential as a stain-free alternative to H&E whole slide images. Fig. 10 shows a set of four TA WSIs with corresponding one-to-one H&E at high magnification. Pathologists are able to analyze these label-free slides at the same magnifications, using the same or similar digital pathology tools as they would with gold standard H&E stained slides. Fig. 10(a) and (b) show whole slide sections of human breast tissue exhibiting invasive mucinous carcinoma and ductal carcinoma, respectively. At both low and high magnifications, irregular and poorly organised ductal structures can be seen in the breast tissue samples, indicative of a pathologic process [3]. Fig. 10(c)

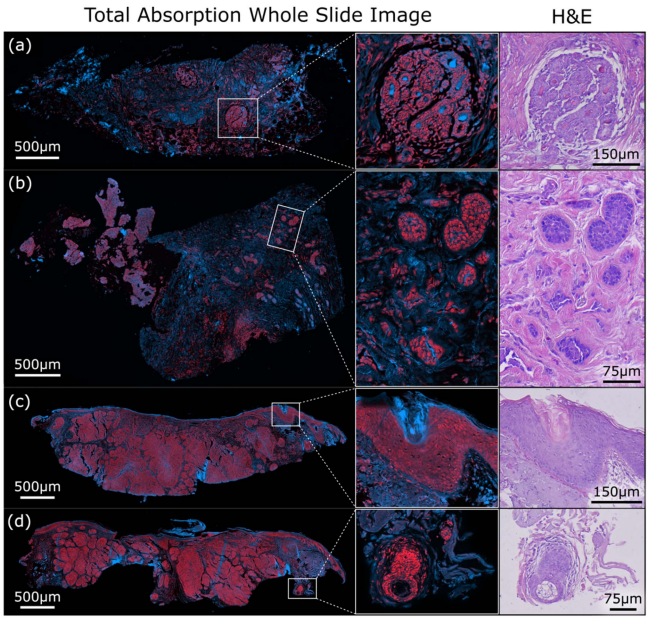

Fig. 10. Four whole slide PARS TA images presented at low and high magnifications with corresponding high magnification H&E images. Parts (a) and (b) show two whole slide images of malignant human breast tissue. Parts (c) and (d) show three PARS whole slide images of malignant human skin tissue.

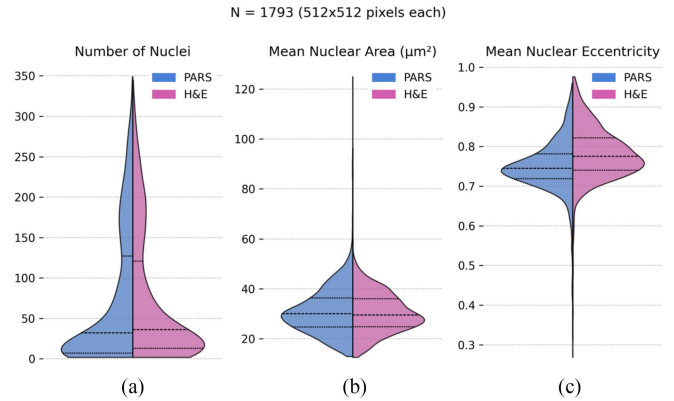

Fig. 11. Feature-based quantitative comparison of the raw PARS images to standard H&E images. A total of N = 1793 image pairs (512 x 512 pixels each) compared based on three metrics (a) Number of nuclei (b) Mean nuclear area and (c) Mean nuclear eccentricity. The dashed horizontal lines in each violin plot indicate the quartiles of the distributions.

and (d) show whole slide sections of human skin tissue exhibiting basal cell carcinoma. At low magnifications, the tumour nodules are easily identifiable in both skin tissue samples as dense nests of basaloid cells primarily below the skin surface with some extending from the epidermis. Of note, the TA colorization heatmap strongly corresponds to and facilitates identifying abnormal areas quickly in comparison to standard H&E images. For reference, the normal epidermis of the skin can be seen at high magnification in Fig. 10(c) along with high resolution details of cell arrangements, nuclei and subnuclear structures. The stratum cornea can be seen primarily with the blue radiative contrast. Furthermore, the high magnification view of Fig. 10(d) shows a sebaceous gland in the tissue sample.

To reinforce the observed visual similarities between the PARS and H&E images, a feature-based quantitative analysis was conducted on a dataset comprising 1793 image pairs, each measuring 512x512 pixels. Images pairs were blindly selected from both breast and skin tissue samples used in this study. Nuclear features, including nuclear count, average nuclear area, and average nuclear eccentricity, were quantified for each image pair (see methods Section II.F).

Fig. 11 illustrates the distributions of these nuclear metrics for both raw PARS and H&E images. The analysis reveals close symmetry in the distributions between each image type, and closely matched median values (center dashed line). Specifically, the median nuclear count, area, and eccentricity for PARS were 32, 30.0μm^2 and 0.74, respectively, while for H&E, these values were 34, 29.5μm^2, and 0.78. The close statistical agreement in nuclear features provides a quantitative assessment specific to histology, suggesting similarity in diagnostically relevant content related to nuclear morphology.

The whole slide scanning times for the PARS point scanning system is primarily a function of the excitation pulse repetition rate (PRR) and the desired pixel spacing (250 nm/pixel), which relates to image magnification. Here, the imaging speed was defined by the 50kHz UV source, resulting in a theoretical limit of 5 min/mm^2 for standard 40x high magnification imaging. Other common magnifications used by pathologists, such as 20x and 10x, correspond to pixel spacings of 500 nm/pixel and 1um/pixel, respectively, which have theoretical imaging times of 1.3 min/mm^2 and 20 s/mm^2, respectively. With this setup, the total scan time for a whole slide image is simply the total scan and autofocus time per section multiplied by the number of sections. Here, each section is of size 0.5 mm $\times$ 0.5 mm and takes approximately 4.7 minutes to scan. This is taking into account the additional time needed for the mechanical stages to accelerate and decelerate while turning around for each row. All 10 axials scans for autofocusing take $\sim$15 seconds per section, representing $\sim$6% of the total section imaging time.

While these imaging times are relatively slow and represent a disadvantage of the current system, there is future possibility for improvement. This can be done with faster repetition rate UV lasers and hybrid optomechanical scanning configurations. For instance, there exist 5.5 MHz pulsed 257 nm UV excitation lasers that could potentially provide up to a $\sim$100x increase in imaging speeds. Future and ongoing work aims to enhance these imaging speeds further with a hybrid optomechanical scanning setup and a similar MHz-range UV excitation source.

D. Whole Slide Virtual H&E Staining

Pathologists are trained to analyze tissue sections stained in the style of H&E, and while the whole slide TA images in Fig. 12 show analogous contrast, emulation of H&E staining style can facilitate a better interpretation experience. Furthermore, machine learning techniques for disease classification and image segmentation have mostly been focused on H&E staining

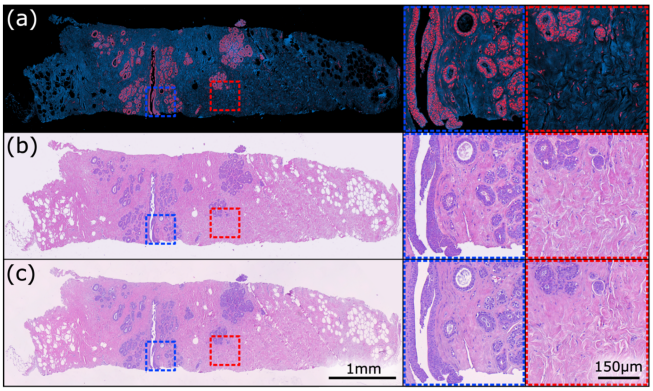

Fig. 12. Comparison between the PARS TA, virtual H&E, and corresponding ground truth H&E whole slide images of a breast needle core biopsy. (a) Shows a raw TA whole slide image. (b) Shows the PARS TA whole slide image virtually stained with H&E. (c) Shows the ground truth H&E whole slide image. Two example areas are shown in higher magnification.

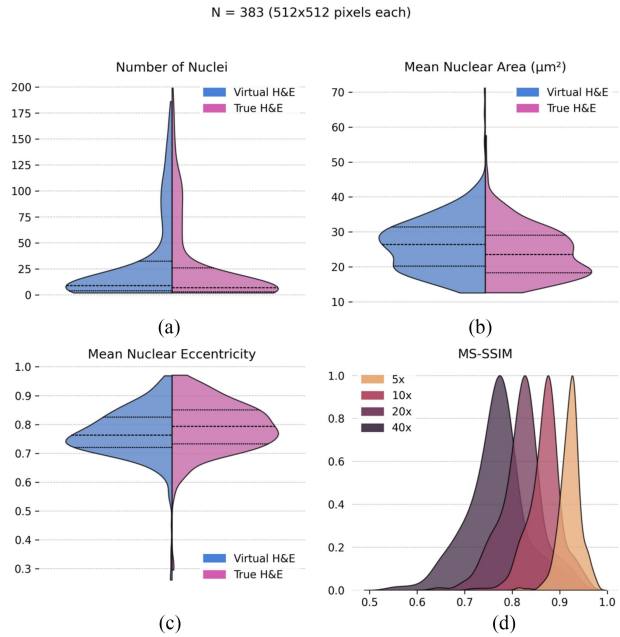

Fig. 13. Quantitative comparison of the virtual H&E and corresponding ground truth H&E WSIs. A feature-based analysis of (a) Number of nuclei (b) Mean nuclear area and (c) Mean nuclear eccentricity is shown. (d) Normalized MS-SSIM distributions computed at increasing magnifications (5x, 10x, 20x and 40x) to provide pixel-level quantitative measure of agreement. The dashed horizontal lines in each violin plot indicate the quartiles of the distributions.

styles [65]. Recently our group has shown such H&E emulation by using the generative machine learning model pix2pix to intelligently combine the radiative, non-radiative and scattering contrast channels [17]. With the automated whole slide scanning system and raw data quality improvements presented here, we are now able to virtually stain whole slide images with H&E. A section of malignant breast tissue, shown in Fig. 12(b), was scanned, and then virtually stained to resemble standard H&E. The virtual H&E model for this sample was trained on a separate whole slide image of breast tissue. Visually, at low magnifications we can see an almost identical whole slide image and are able to make out the same ductal and lobular structures as well as areas of fatty tissue. At high magnifications the virtual H&E staining compares very well to the gold standard, as determined by our clinical colleagues.

As a means of quantitative comparison, the same nuclear features computed in Fig. 11 were calculated here to measure similarity of the virtual and ground truth H&E images. The analysis in Fig. 13(a)–(c) reveals close symmetry in feature distributions and median values for the real and virtual H&E images. Here, the median nuclear count, area, and eccentricity for virtual H&E were 9, 26.36 μm^2 and 0.76, respectively, while for H&E, these values were 7, 23.56 μm^2, and 0.79. Following this, an MS-SSIM metric was computed to measure the pixel-level similarity between the images, shown in Fig. 13(d). MS-SSIM was computed at 40x (native PARS resolution), 20x, 10x, and 5x magnification equivalents with resulting median scores of 0.77, 0.82, 0.87 and 0.92. While these values suggest good structural correspondence between the images, image registration errors and tissue alterations from the staining process may lead to lower values, independent of inherent differences in image modalities. To reliably assess similarity, one must establish diagnostic equivalence through blinded clinical concordance studies. The presented platform and workflow has facilitated such studies [66], by providing pathologists with PARS whole slide images with matching magnification ranges and analogous contrasts to the gold standard H&E.

IV. Conclusion

Here we present an automated PARS whole slide scanning microscope with a refined optics architecture for imaging thin, transmissible samples. The system performs label-free automated whole slide scanning using the autofocus workflow and contrast leveling algorithms presented here. Whole slide images of all three contrast channels (scattering, radiative and non-radiative) were shown in malignant human breast and skin tissue samples. Slides were viewable at magnifications up to 40x and recovered high-resolution subcellular diagnostic details. Clinically relevant features were identified in both the radiative and non-radiative contrast channels as well as in the combined total-absorption (TA) whole slide images. We demonstrated the close correspondence and analogous contrast of the label-free TA images to gold standard H&E staining. Our previously reported pix2pix virtual staining model was successfully applied to an entire breast tissue section, highlighting the system's potential for label-free whole slide H&E emulation. Visual similarities between the PARS, virtual H&E and real H&E images were reinforced with quantitative metrics comparing nuclear features and similarity of structural information. We demonstrated that PARS imaging is non-destructive, permitting standard diagnostic quality H&E staining to be performed sequentially. This ability to capture and virtually stain one-to-one whole slide PARS images is crucial for ongoing blinded clinical pathology validation studies comparing PARS virtual H&E images to ground truth H&E. In future work we aim to capture additional radiative and non-radiative contrasts for improved molecular specificity and emulation of multiple specialized stains.

IV. Disclosures

Authors James Tweel, Benjamin Ecclestone, Deepak Dinakaran, John R. Mackey, and Parsin Haji Reza all have financial interests in IllumiSonics which has provided funding to the PhotoMedicine Labs. Author Marian Boktor does not have any competing interests.

Acknowledgment

The authors thank Dr. Ally-Khan Somani, Dr. Gilbert Bigras and the Cross-Cancer Institute in Edmonton, Alberta for providing human breast and skin tissue samples. The authors also thank Hager Gaouda for helping prepare and stain the tissue samples used in this study.

References

[1] C. E. Day, *Histopathology: Methods and Protocols*, vol. 1180. New York, NY, USA: Springer, 2014, doi: 10.1007/978-1-4939-1050-2.
[2] M. A. Al-Abbadi, "Basics of cytology," *Avicenna J. Med.*, vol. 1, no. 1, pp. 18–28, 2011, doi: 10.4103/2231-0770.83719.
[3] E. Mallon et al., "The basic pathology of human breast cancer," *J. Mammary Gland Biol. Neoplasia*, vol. 5, no. 2, pp. 139–163, Apr. 2000, doi: 10.1023/A:1026439204849.
[4] I. A. Cree et al., "Counting mitoses: SI(ze) matters!," *Modern Pathol.*, vol. 34, no. 9, pp. 1651–1657, 2021, doi: 10.1038/s41379-021-00825-7.
[5] T. S. Gurina and L. Simms, "Histology, staining," *StatPearls, Treasure Island (FL): StatPearls Publishing*, 2023. Accessed: Mar. 24, 2023. [Online]. Available: http://www.ncbi.nlm.nih.gov/books/NBK557663/
[6] J. S. Makki, "Diagnostic implication and clinical relevance of ancillary techniques in clinical pathology practice," *Clin. Med. Insights: Pathol.*, vol. 9, pp. 5–11, Mar. 2016, doi: 10.4137/CPath.S32784.
[7] F. Ghezloo et al., "An analysis of pathologists' viewing processes as they diagnose whole slide digital images," *J. Pathol. Inform.*, vol. 13, Jan. 2022, Art. no. 100104, doi: 10.1016/j.jpi.2022.100104.
[8] E. Mercan et al., "Localization of diagnostically relevant regions of interest in whole slide images," in *Proc. 22nd Int. Conf. Pattern Recognit.*, 2014, pp. 1179–1184, doi: 10.1109/ICPR.2014.212.
[9] B. Bai et al., "Deep learning-enabled virtual histological staining of biological samples," *Light Sci. Appl.*, vol. 12, no. 1, Mar. 2023, Art. no. 57, doi: 10.1038/s41377-023-01104-7.
[10] L. Brown, "Improving histopathology turnaround time: A process management approach," *Curr. Diagn. Pathol.*, vol. 10, no. 6, pp. 444–452, Dec. 2004, doi: 10.1016/j.cdip.2004.07.008.
[11] L. E. Morrison et al., "Conventional histological and cytological staining with simultaneous immunohistochemistry enabled by invisible chromogens," *Lab. Investigation*, vol. 102, no. 5, pp. 545–553, May 2022, doi: 10.1038/s41374-021-00714-2.
[12] A. H. Fischer et al., "Hematoxylin and eosin staining of tissue and cell sections," *CSH Protoc.*, vol. 2008, May 2008, Art. no. pdb.prot4986, doi: 10.1101/pdb.prot4986.
[13] V. Marx, "It's free imaging — Label-free, that is," *Nature Methods*, vol. 16, no. 12, pp. 1209–1212, Dec. 2019, doi: 10.1038/s41592-019-0664-8.
[14] Y. Rivenson et al., "Virtual histological staining of unlabelled tissue-autofluorescence images via deep learning," *Nature Biomed. Eng.*, vol. 3, no. 6, pp. 466–477, Jun. 2019, doi: 10.1038/s41551-019-0362-y.
[15] Y. Zhang et al., "Digital synthesis of histological stains using micro-structured and multiplexed virtual staining of label-free tissue," *Light Sci. Appl.*, vol. 9, no. 1, May 2020, Art. no. 78, doi: 10.1038/s41377-020-0315-y.
[16] Y. Rivenson et al., "PhaseStain: The digital staining of label-free quantitative phase microscopy images using deep learning," *Light Sci. Appl.*, vol. 8, no. 1, Feb. 2019, Art. no. 23, doi: 10.1038/s41377-019-0129-y.
[17] M. Boktor et al., "Virtual histological staining of label-free total absorption photoacoustic remote sensing (TA-PARS)," *Sci. Rep.*, vol. 12, no. 1, Jun. 2022, Art. no. 10296, doi: 10.1038/s41598-022-14042-y.
[18] B. Bai et al.,"Label-free virtual HER2 immunohistochemical staining of breast tissue using deep learning," *BME Front.*, vol. 2022, 2022, Art. no. 9786242, doi: 10.34133/2022/9786242.
[19] F. G. Bechara et al., "Histomorphologic correlation with routine histology and optical coherence tomography," *Skin Res. Technol. Off. J. Int. Soc. Bioeng. Skin ISBS Int. Soc. Digit. Imag. Skin ISDIS Int. Soc. Skin Imag. ISSI*, vol. 10, no. 3, pp. 169–173, Aug. 2004, doi: 10.1111/j.1600-0846.2004.00038.x.
[20] T. Maier et al., "Morphology of basal cell carcinoma in high definition optical coherence tomography: En-face and slice imaging mode, and comparison with histology," *J. Eur. Acad. Dermatol. Venereol.*, vol. 27, no. 1, pp. 97–104, Jan. 2013, doi: 10.1111/j.1468-3083.2012.04551.x.
[21] T. Gambichler et al., "Comparison of histometric data obtained by optical coherence tomography and routine histology," *J. Biomed. Opt.*, vol. 10, no. 4, 2005, Art. no. 44008, doi: 10.1117/1.2039086.
[22] L. P. Hariri et al., "Diagnosing lung carcinomas with optical coherence tomography," *Ann. Amer. Thoracic Soc.*, vol. 12, no. 2, pp. 193–201, Feb. 2015, doi: 10.1513/AnnalsATS.201408-370OC.
[23] G. Popescu, *Quantitative Phase Imaging of Cells and Tissues*, 1st ed., New York, NY, USA: McGraw-Hill Education, 2011. [Online]. Available: https://www.accessengineeringlibrary.com/content/book/9780071663427
[24] Y. N. Nygate et al., "Holographic virtual staining of individual biological cells," *Proc. Nat. Acad. Sci. United States Amer.*, vol. 117, no. 17, pp. 9223–9231, Apr. 2020, doi: 10.1073/pnas.1919569117.
[25] Z. Wang et al., "Tissue refractive index as marker of disease," *J. Biomed. Opt.*, vol. 16, no. 11, Nov. 2011, Art. no. 116017, doi: 10.1117/1.3656732.
[26] S. L. Jacques, "Optical properties of biological tissues: A review," *Phys. Med. Biol.*, vol. 58, no. 11, pp. 37–61, Jun. 2013, doi: 10.1088/0031-9155/58/11/R37.
[27] J. Xia, J. Yao, and L. V. Wang, "Photoacoustic tomography: Principles and advances," *Electromagn. Waves*, vol. 147, pp. 1–22, 2014.
[28] F. Jamme et al., "Deep UV autofluorescence microscopy for cell biology and tissue histology," *Biol. Cell*, vol. 105, no. 7, pp. 277–288, 2013, doi: 10.1111/boc.201200075.
[29] N. H. Patterson et al., "Autofluorescence microscopy as a label-free tool for renal histology and glomerular segmentation," 2021, *arXiv:07.16.452703*.
[30] Y. K. Tao et al., "Assessment of breast pathologies using nonlinear microscopy," *Proc. Nat. Acad. Sci. United States Amer.*, vol. 111, no. 43, pp. 15304–15309, Oct. 2014, doi: 10.1073/pnas.1416955111.
[31] S. Witte et al., "Label-free live brain imaging and targeted patching with third-harmonic generation microscopy," *Proc. Nat. Acad. Sci. United States Amer.*, vol. 108, no. 15, pp. 5970–5975, Apr. 2011, doi: 10.1073/pnas.1018743108.
[32] M. Ji et al., "Rapid, label-free detection of brain tumors with stimulated Raman scattering microscopy," *Sci. Transl. Med.*, vol. 5, no. 201, Sep. 2013, Art. no. 201ra119, doi: 10.1126/scitranslmed.3005954.
[33] F. - K. Lu et al., "Label-free DNA imaging in vivo with stimulated Raman scattering microscopy," *Proc. Nat. Acad. Sci. United States Amer.*, vol. 112, no. 37, pp. 11624–11629, Sep. 2015, doi: 10.1073/pnas.1515121112.
[34] D. A. Orringer et al., "Rapid intraoperative histology of unprocessed surgical specimens via fibre-laser-based stimulated Raman scattering microscopy," *Nature Biomed. Eng.*, vol. 1, no. 2, Feb. 2017, Art. no. 0027, doi: 10.1038/s41551-016-0027.
[35] H. Tu et al., "Stain-free histopathology by programmable supercontinuum pulses," *Nature Photon.*, vol. 10, no. 8, pp. 534–540, Aug. 2016, doi: 10.1038/nphoton.2016.94.
[36] S. You et al., "Intravital imaging by simultaneous label-free autofluorescence-multiharmonic microscopy," *Nature Commun.*, vol. 9, no. 1, May 2018, Art. no. 2125, doi: 10.1038/s41467-018-04470-8.
[37] A. C. Croce and G. Bottiroli, "Autofluorescence spectroscopy and imaging: A tool for biomedical research and diagnosis," *Eur. J. Histochemistry*, vol. 58, no. 4, Dec. 2014, Art. no. 2461, doi: 10.4081/ejh.2014.2461.
[38] M. Monici, "Cell and tissue autofluorescence research and diagnostic applications," *Biotechnol. Annu. Rev.*, vol. 11, pp. 227–256, 2005, doi: 10.1016/S1387-2656(05)11007-2.
[39] Y. - C. Chen et al., "Laser-emission imaging of nuclear biomarkers for high-contrast cancer screening and immunodiagnosis," *Nature Biomed. Eng.*, vol. 1, no. 9, pp. 724–735, Sep. 2017, doi: 10.1038/s41551-017-0128-3.
[40] T. Kobayashi et al., "Label-free imaging of melanoma with confocal photothermal microscopy: Differentiation between malignant and benign tissue," *Bioengineering*, vol. 5, no. 3, Aug. 2018, Art. no. 67, doi: 10.3390/bioengineering5030067.
[41] M. Schnell et al., "All-digital histopathology by infrared-optical hybrid microscopy," *Proc. Nat. Acad. Sci. United States Amer.*, vol. 117, no. 7, pp. 3388–3396, Feb. 2020, doi: 10.1073/pnas.1912400117.

[42] R. Cao et al., "Label-free intraoperative histology of bone tissue via deep-learning-assisted ultraviolet photoacoustic microscopy," *Nature Biomed. Eng.*, vol. 7, no. 2, pp. 124–134, Feb. 2023, doi: 10.1038/s41551-022-00940-z.

[43] D. - K. Yao et al., "Optimal ultraviolet wavelength for in vivo photoacoustic imaging of cell nuclei," *J. Biomed. Opt.*, vol. 17, no. 5, May 2012, Art. no. 056004, doi: 10.1117/1.JBO.17.5.056004.

[44] C. Zhang et al., "Label-free photoacoustic microscopy of cytochromes," *J. Biomed. Opt.*, vol. 18, no. 2, Feb. 2013, Art. no. 020504, doi: 10.1117/1.JBO.18.2.020504.

[45] N. J. M. Haven et al., "Ultraviolet photoacoustic remote sensing microscopy," *Opt. Lett.*, vol. 44, no. 14, pp. 3586–3589, Jul. 2019, doi: 10.1364/OL.44.003586.

[46] S. Abbasi et al., "All-optical reflection-mode microscopic histology of unstained human tissues," *Sci. Rep.*, vol. 9, no. 1, Sep. 2019, Art. no. 13392, doi: 10.1038/s41598-019-49849-9.

[47] P. Hajireza et al., "Non-interferometric photoacoustic remote sensing microscopy," *Light Sci. Appl.*, vol. 6, no. 6, Jun. 2017, Art. no. e16278, doi: 10.1038/lsa.2016.278.

[48] B. S. Restall et al., "In vivo combined virtual histology and vascular imaging with dual-wavelength photoacoustic remote sensing microscopy," *OSA Continuum*, vol. 3, no. 10, pp. 2680–2689, Oct. 2020, doi: 10.1364/OSAC.398269.

[49] Z. Hosseinaee et al., "Functional and structural ophthalmic imaging using noncontact multimodal photoacoustic remote sensing microscopy and optical coherence tomography," *Sci. Rep.*, vol. 11, no. 1, Jun. 2021, Art. no. 11466, doi: 10.1038/s41598-021-90776-5.

[50] Z. Hosseinaee et al., "Functional photoacoustic remote sensing microscopy using a stabilized temperature-regulated stimulated Raman scattering light source," *Opt. Exp.*, vol. 29, no. 19, pp. 29745–29754, Sep. 2021, doi: 10.1364/OE.434004.

[51] L. Mukhangaliyeva et al., "Deformable mirror-based photoacoustic remote sensing (PARS) microscopy for depth scanning," *Biomed. Opt. Exp.*, vol. 13, no. 11, pp. 5643–5653, Nov. 2022, doi: 10.1364/BOE.471770.

[52] K. Bell et al., "Reflection-mode virtual histology using photoacoustic remote sensing microscopy," *Sci. Rep.*, vol. 10, no. 1, Nov. 2020, Art. no. 19121, doi: 10.1038/s41598-020-76155-6.

[53] B. R. Ecclestone et al., "Improving maximal safe brain tumor resection with photoacoustic remote sensing microscopy," *Sci. Rep.*, vol. 10, no. 1, Oct. 2020, Art. no. 17211, doi: 10.1038/s41598-020-74160-3.

[54] K. Bell et al., "Hyperspectral absorption microscopy using photoacoustic remote sensing," *Opt. Exp.*, vol. 29, no. 15, pp. 24338–24348, Jul. 2021, doi: 10.1364/OE.430403.

[55] P. Kedarisetti et al., "Label-free lipid contrast imaging using non-contact near-infrared photoacoustic remote sensing microscopy," *Opt. Lett.*, vol. 45, no. 16, pp. 4559–4562, Aug. 2020, doi: 10.1364/OL.397614.

[56] B. R. Ecclestone et al., "Label-free complete absorption microscopy using second generation photoacoustic remote sensing," *Sci. Rep.*, vol. 12, no. 1, May 2022, Art. no. 8464, doi: 10.1038/s41598-022-11235-3.

[57] B. D. Cikaluk et al., "Rapid ultraviolet photoacoustic remote sensing microscopy using voice-coil stage scanning," *Opt. Exp.*, vol. 31, no. 6, pp. 10136–10149, Mar. 2023, doi: 10.1364/OE.481313.

[58] M. T. Martell et al., "Deep learning-enabled realistic virtual histology with ultraviolet photoacoustic remote sensing microscopy," *Nature Commun.*, vol. 14, no. 1, Sep. 2023, Art. no. 5967, doi: 10.1038/s41467-023-41574-2.

[59] D. - K. Yao et al., "*In vivo* label-free photoacoustic microscopy of cell nuclei by excitation of DNA and RNA," *Opt. Lett.*, vol. 35, no. 24, pp. 4139–4141, Dec. 2010, doi: 10.1364/OL.35.004139.

[60] T. Yeo, S. On, and R. Sinniah, "Autofocusing for tissue microscopy," *Image Vis. Comput.*, vol. 11, no. 10, pp. 629–639, Dec. 1993, doi: 10.1016/0262-8856(93)90059-P.

[61] U. Schmidt, "Cell Detection with Star-Convex Polygons," in *Medical Image Computing and Computer Assisted Intervention – MICCAI 2018*, A. F. Frangi Ed. Cham, Switzerland: Springer International Publishing, 2018, pp. 265–273, doi: 10.1007/978-3-030-00934-2_30.

[62] G. Landini, G. Martinelli, and F. Piccinini, "Colour deconvolution: Stain unmixing in histological imaging," *Bioinformatics*, vol. 37, no. 10, pp. 1485–1487, Jun. 2021, doi: 10.1093/bioinformatics/btaa847.

[63] T. L. Sellaro et al., "Relationship between magnification and resolution in digital pathology systems," *J. Pathol. Inform.*, vol. 4, no. 1, Jan. 2013, Art. no. 21, doi: 10.4103/2153-3539.116866.

[64] C. H. Richards et al., "The prognostic value of histological tumor necrosis in solid organ malignant disease: A systematic review," *Future Oncol.*, vol. 7, no. 10, pp. 1223–1235, Oct. 2011, doi: 10.2217/fon.11.99.

[65] J. van der Laak, G. Litjens, and F. Ciompi, "Deep learning in histopathology: The path to the clinic," *Nature Med.*, vol. 27, no. 5, pp. 775–784, May 2021, doi: 10.1038/s41591-021-01343-4.

[66] J. E. D. Tweel et al., "Photon absorption remote sensing imaging of breast needle core biopsies is diagnostically equivalent to gold standard h&e histologic assessment," *Curr. Oncol.*, vol. 30, no. 11, pp. 9760–9771, Nov. 2023, doi: 10.3390/curroncol30110708.